International Forum on Aeroelasticity and Structural Dynamics
IFASD 2024
17-21 June 2024, The Hague, The Netherlands

# AEROSERVOELASTIC MODELS FOR DESIGN, TESTING, FLIGHT TEST CLEARANCE AND VALIDATION OF ACTIVE FLUTTER SUPPRESSION CONTROL LAWS

**Thiemo M. Kier[1], Matthias Wüstenhagen[1], Özge Süelözgen[1], Ramesh Konatala[1], Yasser Meddaikar[2], Keith Soal[2], Nicolas Guerin[3], Julius Bartasevicius[4], Bálint Patartics[5], Béla Takarics[5], Bálint Vanek[5]**

[1]German Aerospace Center DLR, Institute of System Dynamics and Control
Münchener Str. 20, 82234 Weßling, Germany
Thiemo.Kier@dlr.de

[2]German Aerospace Center DLR, Institute of Aeroelasticity
Bunsenstr. 10, 37073 Göttingen, Germany

[3]The French Aerospace Lab ONERA, Aerodynamics Aeroelasticity Acoustics Department
29 Av. de la Division Leclerc, 92320 Châtillon, France

[4]Technical University of Munich TUM, Chair of Aircraft Design
Boltzmannstr. 15, 85748 Garching, Germany

[5]Institute for Computer Science and Control SZTAKI
Kende u. 13-17, 1111, Budapest, Hungary

**Keywords:** integrated aeroservoelastic simulation models, ASE, active flutter suppression, AFS, control law design, flight test clearance

**Abstract:** One of the main objectives of the EU funded project FliPASED, was to mature the technology of Active Flutter Suppression (AFS). At the end of the project, such an AFS system was designed, implemented and successfully demonstrated in flight. The flutter control laws suppressed a classical symmetric wing bending-torsion flutter mechanism of the demonstrator aircraft and extended the flight envelope by over 10% beyond open loop flutter speed.

This paper addresses the aeroservoelastic model development from design to the final test flight during the course of the project. Mathematical models were involved throughout the development axis of the demonstrator and the AFS system. The wing design was supported with flutter analyses. Models for control law synthesis of the primary flight control as well as the flutter control function were provided. Software and Hardware in the loop (SIL/HIL) simulations were set up to validate the control law design.

Data from ground tests was used to update the simulation models. In particular the availability of data from the ground vibration test substantially improved the prediction of the open loop flutter speed. The updated models were then used for flight test clearance of the active flutter control laws. Online and post-flight data analysis validated the models and showed excellent agreement.

A formalized modelling process for generating consistent simulation and analysis models for various design applications in the field of aeroservoelasticity and their the specific requirements is presented.

## 1 INTRODUCTION

Improving the aerodynamic efficiency of aircraft with high aspect ratio wings is a current trend for future designs. However, the slender wing structures are prone to suffer from an adverse interaction between aerodynamics and structural dynamics causing a destructive instability called flutter. Active Flutter Suppression (AFS) is a key technology to enable high aspect ratio wings by stabilizing the flutter behavior without weight penalties using an active control system. The EU funded projects FLEXOP (Flutter Free Flight Envelope Expansion for Economical Performance Improvement) and FliPASED (Flight Phase Adaptive Aero-Servo-Elastic Aircraft Design Methods) addressed this topic and matured the technology up to a successful demonstration of the AFS control laws in flight tests with the P-FLEX UAV.

Accurate simulation models of the closed loop flexible airframe including sensor and actuator dynamics are essential for the design and successful demonstration of such an AFS system. This paper addresses the development of such mathematical models, their validation and enrichment with available data along the project progress timeline.

The mathematical models are employed for various different design activities. Linear low order models are required for model-based control law design. This applies to the baseline controller and autopilot functions, as well as the flutter suppression control laws. Their validation is then performed with an integrated simulation containing nonlinear flight dynamics, flexible structure and unsteady aerodynamics. During the development various design analyses, e.g. flutter analysis with and without the AFS active need to be performed. Realtime capable models are required for hardware in the loop tests to validate controller implementations with adequate sensor and actuator characteristics including system delays. Finally, flight test clearance of the control laws must be performed to ensure safe operation during flight tests.

As the project progresses, available test data is used to improve the simulation models. A Ground Vibration Test (GVT) was performed to update the modal frequencies, shapes and damping. Flight test clearance of the active flutter suppression control laws was conducted using these updated models. Online and post flight modal identification was used to confirm the open loop flutter speed predictions during subcritical flight tests. These test results served as final validation of the simulation model to clear the AFS control laws for the successful demonstration beyond the open loop flutter speed.

This paper describes the dynamic aircraft model integration process (DAMIP) and its application to the demonstrator aircraft for the various design activities mentioned. These aeroservoelastic models can be adapted for different design analyses, while still ensuring consistency due to a modular approach in the model integration, i.e. the governing equations are adapted to the respective task using the same underlying data.

## 2 DEMONSTRATOR AIRCRAFT

The P-FLEX demonstrator with which the active flutter suppression control laws were demonstrated is a successor of the T-FLEX aircraft. T-FLEX was lost during a loss of reception event, which triggered the flight termination system. The aircraft was rebuilt in winter 2022/2023 and features similar specifications, a design take-off mass of 65 kg, a 7.08 m wing span with a 20 deg sweepback angle. The wing area is 2.54 $m^2$ which amounts to an aspect ratio of around 19.8. The aircraft is powered by a 300 N jet engine (AeroDesignWorks B300F), which is controlled by the autopilot modes to maintain a preselected speed. Overall, there are twelve control surfaces, four ruddervators at the V-tail for pitch and yaw control and four flaps on each wing,

where the inner two are used mainly for high lift configuration during start and landing, flap 3 is used for roll control by the baseline flight controller and the outermost flap 4 is used for active flutter suppression system. Flap 4 is equipped with a heavy, high bandwidth actuator to fulfill the frequency requirements for active flutter suppression control. Flutter rods are mounted inboard of flap 4. These rods facilitate a mass at their tips that lowers the torsional modal frequencies and reduce the flutter speed to around 50 m/s and therefore within the flight envelope. As a safety measure, the flutter masses are spring loaded and can be released to rapidly shift forward to the trailing edge to obtain a flutter free configuration (i.e. a flutter speed beyond 70 m/s).

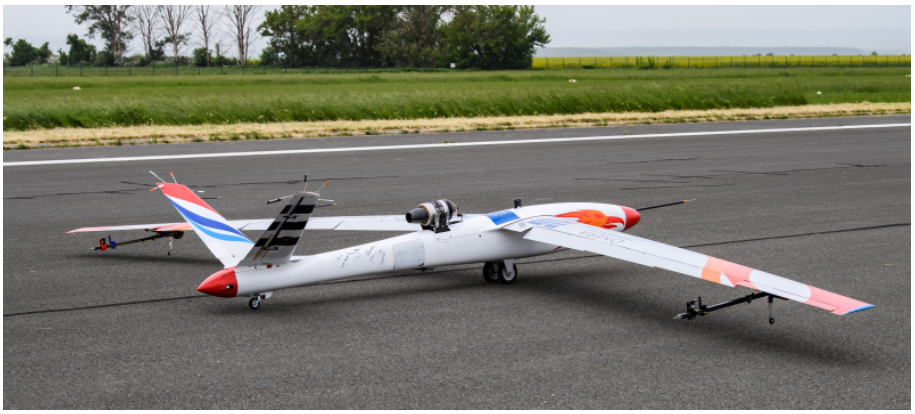

Figure 1: Demonstrator aircraft P-FLEX on the runway of EDBC airport

The aircraft is equipped with the following sensors for primary flight control: a central fuselage mounted IRS (inertial reference system) for GPS coordinates and inertial parameters (accelerations and angles) and an airdata boom for measuring the aerodynamic angle of attack and sideslip, airspeed and pressures. Twelve IMUs at the front and rear spar at 30%, 60% and 90% span locations are installed to capture translational accelerations and rotational rates of the dynamic flexible deformation of the aircraft. [1]

## 3 MODELLING PROCESS

Now the task is to build mathematical models of the demonstrator for the various applications during the course of the project. Generally, such multi-disciplinary flight dynamics models of rigid and flexible aircraft are needed in various areas and stages of the aircraft design process, like for example for flight loads, flutter analysis and flight control law design. These models must be sufficiently accurate, but also allow for a multitude of simulations in a reasonable amount of time, i.e. the models must be 'loop-capable'. Depending on the application, flight dynamics models need to be available in various forms, like ODEs for nonlinear simulation, linear state space models for control synthesis and analysis, etc. A major challenge in development of such multi-disciplinary flight dynamics models is the handling and integration of data from various sources, removing overlaps, and filling in gaps in case specific data is missing. The DLR Institute of System Dynamics and Control has developed methods and tools for these tasks and established a model integration process called DAMIP (Dynamic Aircraft Model Integration Process) to cover these aforementioned aspects of the generation of simulation and analysis models [2]. The process is organized in 5 stages as shown in figure 2. Some of these steps will be exemplified for the demonstrator aircraft in this section.

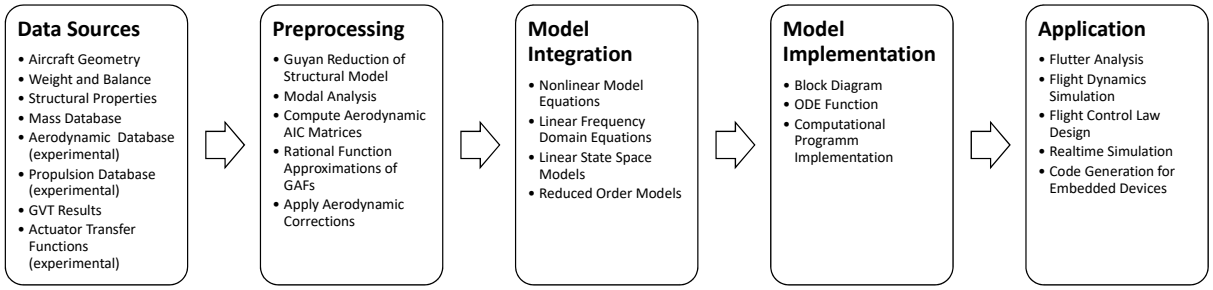


Figure 2: Dynamic Aircraft Model Integration Process

### 3.1 Data Sources and Preprocessing

For setting up suitable simulation models, pertinent data needs to be provided. This data must be preprocessed to make it suitable for use in the mathematical model equations. Some examples of such a preprocessing of the data sources are listed below.

The Technical University of Munich designed the flutter wing using a very detailed FEM model representation of the structural features. Figure 3 shows the wing-to-fuselage joint and the outer wing segment with the actuator mount as well as the flutter rods.

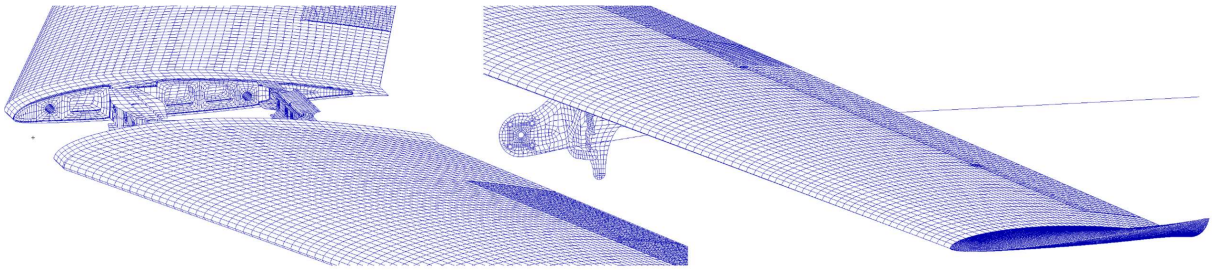

Figure 3: Detailed FEM model of the flutter wing

In the preprocessing step the detailed wing FEM is reduced using a static condensation method according to Guyan [3] from several 100.000 degrees of freedom to a couple of 100 along a reference axis for the wingbox and the individual control surfaces. The remainder of the aircraft, i.e. the fuselage and the empennage are modelled by beams to represent their structural dynamic properties. The details for on this pre-process can be found in [4]. Later, the structural dynamics model was updated using experimental data from the static and ground vibration tests.

With the CAD geometry, steady CFD data was generated for various angles of attack. The CFD data constituted an aerodynamic database that was updated during the course of the project. The aerodynamics of the mathematical model is based on the unsteady Doublet Lattice Method and the CFD data was used to correct for unmodelled effects of the potential flow based DLM matrices. Furthermore, the CFD data and other aerodynamic methods were used obtain a drag polar. This is particularly important for flight dynamics simulations, as the drag has substantial impact on flight dynamic modes such as the phugoid.

Experimental data from HIL test benches is used to characterize the dynamic behavior and system delays of the actuators. This actuator data is then cast in a second order transfer function with the corresponding rate and position limits. Also the dynamic data of the engine test bench was used to set up a low order dynamic engine model.

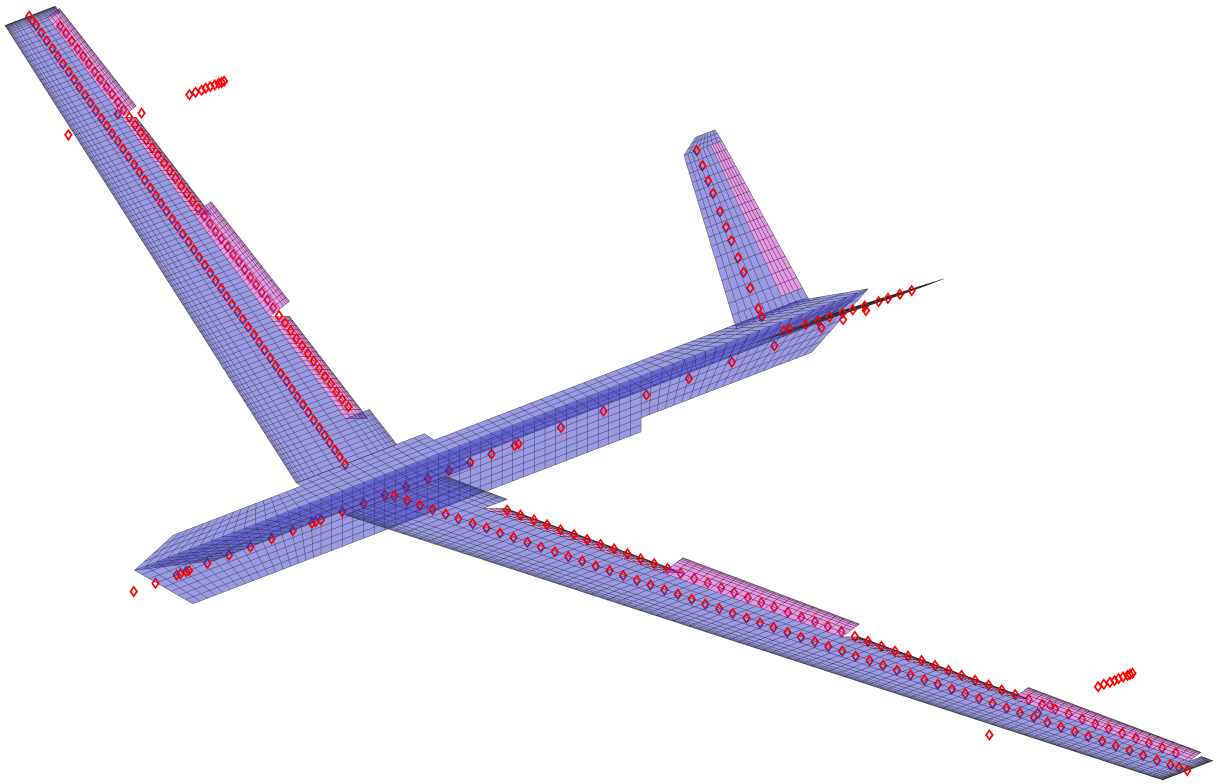

Figure 4: Integrated Model: structural nodes (red), DLM panels (blue) and the associated control surfaces (pink)

### 3.2 Model Integration and Implementation

The model integration refers to the actual mathematical equations used to setup the model. These equations might be application dependent, as the model needs to satisfy the necessities of the particular analysis at hand. Further details of the various applications of the models will be covered in the next sections. Once a set of suitable model equations has been selected, the model can be implemented in different environments, depending on the application. To this end various model implementation approaches can be used, ranging from programmatic implementation e.g. for frequency domain flutter analysis, explicit nonlinear ODEs (ordinary differential equations) functions that can be integrated in time, to block diagrams such as Simulink models, which in turn can be used to generate code for embedded devices like the Flight Control Computer (FCC).

### 3.3 Model Application

The applications during the course of the projects FLEXOP and FliPASED are mainly focused on the development and testing of the active flutter suppression system. Hence, open loop and closed loop flutter analysis plays a key role. Furthermore, control law synthesis and analysis for primary flight control laws and autopilot modes, as well as the for flutter control laws are the primary design tasks. The interaction of the various control functions need to be assessed in software in the loop simulations. Real time capable simulation of the aeroelastic models for HIL testing of flight hardware and the implemented control laws are required. GVT updated models are of particular interest for pre-flight flutter analysis and flight test clearance of the active suppression control laws. Finally, the models and the AFS control laws were validated using flight test data.

## 4 NONLINEAR SIMULATION MODEL

The following section describes the model integration process of the nonlinear flexible aircraft in more detail, i.e., the structural model, the equations of motion, the external forces due to propulsion and the aerodynamics, and the flight control system. These equations are integrated in the loads environment VarLoads [5] and are expressed in closed form by the use of AIC matrices, i.e., no iteration between the structural and the aerodynamic model is necessary. More information on the model integration can be found in [6]. This nonlinear model serves as basis for the derived models for specialized applications that will be explained in later sections.

### 4.1 Structural Dynamics and Equations of Motion

The starting point when setting up the equations of motion for a simulation model of a flexible aircraft is an Finite Element Model (FEM). The static condensation process has been described previously, where condensation points ($g-set$) were placed along a loads reference axes, cf. figure 4. The mass of the primary structure, which was modelled with density of the elements is obtained from the condensation process. The system masses and unmodelled structure are directly connected to the $g-set$ points as concentrated mass elements. Subsequently a modal analysis is carried out and only part of the modal basis is retained to further reduce the model size and computational cost. The accuracy of the condensation process can be assessed by evaluating the MAC (Modal Assurance Critria) values of the mode shapes of the full model versus the reduced model.

The eigenvalues and eigenvectors define the generalized coordinates of the $h-set$. The zero eigenvalues represent the rigid body motion. The $h-set$ can be partitioned into six rigid body DoFs ($b-set$) and a flexible part ($f-set$). The rigid body mode shapes $\mathbf{\Phi}_{gb}$ and the retained modes of the eigenvector matrix $\mathbf{\Phi}_{gf}$ are used to generalized the equations of motion, which are given in the frequency domain by

$$\left\{ -\omega^2 \begin{bmatrix} \mathbf{M}_{bb} & \mathbf{0} \\ \mathbf{0} & \mathbf{M}_{ff} \end{bmatrix} + \mathrm{j}\,\omega \begin{bmatrix} \mathbf{0} & \mathbf{0} \\ \mathbf{0} & \mathbf{B}_{ff} \end{bmatrix} + \begin{bmatrix} \mathbf{0} & \mathbf{0} \\ \mathbf{0} & \mathbf{K}_{ff} \end{bmatrix} \right\} \begin{bmatrix} \mathbf{u}_b \\ \mathbf{u}_f \end{bmatrix} = \begin{bmatrix} \mathbf{\Phi}_{gb}^{\mathrm{T}} \\ \mathbf{\Phi}_{gf}^{\mathrm{T}} \end{bmatrix} \mathbf{P}_g^{ext}(\omega). \tag{1}$$

Note that the rigid body $b-set$ DoFs in eq. (1) are defined in a earth fixed coordinate frame.

A suitable set of equations of motion to account for large rigid body motions and linear flexibility is derived in the references [7, 8]. The nonlinear equations of motion describe the movement relative to a "mean axes" body reference frame. Equations of motion for an unrestrained flexible aircraft accounting for large rigid body motions are given by

$$\begin{aligned} \begin{bmatrix} \mathbf{m}_b \left( \dot{\mathbf{V}}_b + \mathbf{\Omega}_b \times \mathbf{V}_b - \mathbf{T}_{bE}\, \mathbf{g}_E \right) \\ \mathbf{J}_b \dot{\mathbf{\Omega}}_b + \mathbf{\Omega}_b \times (\mathbf{J}_b \mathbf{\Omega}_b) \end{bmatrix} &= \mathbf{\Phi}_{gb}^{\mathrm{T}} \mathbf{P}_g^{\mathrm{ext}}(t) \\ \mathbf{M}_{ff} \ddot{\mathbf{u}}_f + \mathbf{B}_{ff} \dot{\mathbf{u}}_f + \mathbf{K}_{ff} \mathbf{u}_f &= \mathbf{\Phi}_{gf}^{\mathrm{T}} \mathbf{P}_g^{\mathrm{ext}}(t), \end{aligned} \tag{2}$$

where $\mathbf{\Phi}_{gb}$ is the rigid body modal matrix about the center of gravity and in directions as customary in flight mechanics, i.e., x-forward, z-down. $\mathbf{V}_b$ and $\mathbf{\Omega}_b$ are the velocity and angular velocity vectors, respectively in the body frame of reference. The matrix $\mathbf{T}_{bE}$ transforms the gravitational vector from an earth fixed ($E$) to the body fixed coordinate frame ($b$) as a function of Euler angles.

### 4.2 Aerodynamic Model

The major contribution to the external forces apart from the propulsion forces stem from the aerodynamics. So called Aerodynamic Influence Coefficient (AIC) matrices based on linear

potential flow theory have classically been used for aeroelastic applications. The AIC matrices represent a linear relationship between the normalwash at the control point to the panel pressure, i.e., a change of the flow, normal to the panel surface at control point results in a change in pressure distribution. This allows to easily account for flexible deformation, which are simply treated as change in the normalwash vector $\mathbf{w}_j$.

The pressure coefficients are computed by

$$\Delta \mathbf{c_p}_j = \mathbf{Q}_{jj}\ \mathbf{w}_j, \tag{3}$$

where $\mathbf{Q}_{jj}$ is the so called AIC matrix. Traditionally, the Vortex Lattice and the Doublet Lattice Methods are used to obtain these AIC matrices. The Doublet Lattice Method provides the complex valued AIC matrix as function of reduced frequency $k = \frac{c_{ref}/2}{U_\infty}\omega$, which describe the unsteady aerodynamic transfer functions. In frequency domain calculations the complex AICs can be used directly. For time domain simulations, a Rational Function Approximation (RFA) [6, 9] is required to transform the AICs to the Laplace domain. The rational functions can then be cast in the form of a system of linear ordinary differential equations amenable to time integration.

The load transformation to panel reference point is done by integrating the pressures, which is mostly a simple multiplication with the aerodynamic box area. In some classical aerodynamic panel methods, additional moments occur due to an offset between control point and pressure application point, cf. [10]. These are accounted for by introducing rotational degrees of freedom in the aerodynamic panel $(k-set)$ and the respective moment arms into the integration matrix $\mathbf{S}_{kj}$. Multiplication with the dynamic pressure yields the aerodynamic forces.

$$\mathbf{P}_k^{\text{aero}} = q_\infty\ \mathbf{S}_{kj}\ \mathbf{c_p}_j \tag{4}$$

Next, the boundary condition for the normalwash has to be considered:

$$\mathbf{w}_j(k) = \left(\mathbf{D^x}_{jk} + \frac{\mathrm{d}}{\mathrm{d}t}\left(\frac{c_{ref}/2}{U_\infty}\right)\cdot\ \mathbf{D^t}_{jk}\right)\ \mathbf{u}_k(t), \tag{5}$$

where the matrix $\mathbf{D^x}_{jk}$ accounts for a change in downwash due to tilting of the normal vector with respect to the free stream direction and the matrix $\mathbf{D^t}_{jk}$ for additional downwash due to movement of the boundary in direction of the panel normal. The factor $\frac{c_{ref}/2}{U_\infty}$ in equation (5) is needed due to the conversion from reduced to natural frequency. The vector $\mathbf{u}_k(t)$ represents the motion of the aerodynamic reference points.

In the nonlinear equations of motion, the vectors $\mathbf{V}_b$ and $\mathbf{\Omega}_b$ are defined in a body fixed frame of reference. Hence, the steady deflection of rigid body modes does not induce aerodynamic loads. Therefore, the differentiation matrix $\mathbf{D^x}$ needs to be omitted for the rigid body modes.

Finally, the aerodynamic loads have to be mapped to the structural degrees of freedom. The matrix connecting the displacements of the structural grid $(g-set)$ to the aerodynamic grid $(k-set)$ is called spline matrix $\mathbf{T}_{kg}$.

$$\mathbf{u}_k = \mathbf{T}_{kg}\mathbf{u}_g \tag{6}$$

This mapping is achieved by, e.g., employing radial basis functions such as the commonly used Infinite Plate Spline (IPS) [11]. The aerodynamic loads can be mapped back onto the structure with the transpose of the spline matrix, based on the principal of virtual work.

$$\mathbf{P}_g^{\text{aero}} = \mathbf{T}_{kg}^{\mathrm{T}}\mathbf{P}_k^{\text{aero}} \tag{7}$$

Similarly, the modal matrix $\mathbf{\Phi}_{gf}$ and its transpose connect the flexible part of the equations of motion (1) and (2) to the aerodynamic model.

### 4.3 Rational Function Approximation

The Doublet Lattice Method [12] provides aerodynamic matrices as tabulated values at discrete reduced frequencies. One possibility to make them amenable for time domain integration is the so called rational function approximation (RFA), where the frequency domain transfer functions are fit with suitable "rational" terms. These can then be Laplace transformed and cast in state space form. Many flavors of this method have been published in literature [9, 13, 14]. In most of these publications the approximation is applied to the generalized aerodynamic matrices $\mathbf{Q}_{hh}$, i.e. the AIC matrices are already post-multiplied with the differentiation matrices (5) and the modal basis.

In [6] an RFA fit of the AICs $\mathbf{Q}_{jj}(k)$ without prior multiplication with differentiation matrices was proposed, the so called "physical" RFA:

$$\mathbf{Q}_{jj}(\hat{s}) = \mathbf{Q^0}_{jj} + \mathbf{Q^1}_{jj}\hat{s} + \sum_{i=1}^{n_p} \mathbf{Q^{L}}_{i\,jj} \frac{\hat{s}\mathbf{I}}{\hat{s} + p_i}, \tag{8}$$

where $\hat{s} = s\left(\frac{c_{ref}/2}{U_\infty}\right)$ is the Laplace domain equivalent to the reduced frequency $k$. The reason for the presence of a second derivative in the classical RFA compared to the present formulation, is the additional time derivative in the downwash equation (5). The present, "physical" RFA (8) has several advantages over the approximation of the generalized aerodynamic forces, e.g., the fit is not tied to a particular mass case. But more importantly, the individual terms of the fit allow a physical interpretation: The term $\mathbf{Q^0}_{jj}$ represents the quasi-steady term, $\mathbf{Q^1}_{jj}$ is the added mass (in incompressible flow), and the terms $\mathbf{Q^{L}}_{i\,jj}$ with the predefined poles $p_i$, are responsible for the lagging behavior of the unsteady flow.

Since the input to the physical RFA is defined on the control point level, the gust velocity and the time lags associated with the penetration speed can be applied directly. The problematic approximation of the gust column can be omitted completely. Further, this fit also allows the consideration of a nonlinear position dependence of the wind field as demonstrated in [15], since the normalwash $\mathbf{w}_j$ can be computed online and fed into a realization of the ordinary differential equations (ODE) (9) of the unsteady aerodynamics in order to determine the so called lag states $\mathbf{x}_L$.

$$\dot{\mathbf{x}}_L = \tfrac{U_\infty}{c_{ref}/2}\mathbf{R}\,\mathbf{x}_L + \mathbf{E}\,\dot{\mathbf{w}}_j \tag{9}$$

The matrices $\mathbf{R}$ and $\mathbf{E}$ are stacked diagonal matrices, containing the poles $p_i$, respectively identity matrices. The splined aerodynamic forces including steady the unsteady parts are then

$$\mathbf{P}_g^{aero} = \underbrace{\left(\mathbf{Q^0}_{gj}\,\mathbf{w}_j\right)}_{\text{steady } \mathbf{P}_g^s(\mathbf{w}_j)} + \underbrace{\left(\mathbf{Q^1}_{gj}\left(\tfrac{c_{ref}/2}{U_\infty}\right)\,\dot{\mathbf{w}}_j + \mathbf{D}\,\mathbf{x}_L(\dot{\mathbf{w}}_j)\right)}_{\text{unsteady } \mathbf{P}_g^u(\dot{\mathbf{w}}_j)}, \tag{10}$$

where $\mathbf{D}$ contains the coefficients $\mathbf{Q^{L}}_{i\,gj}$ from the least squares procedure according to Roger [9]. With the "physical" RFA it is possible to discern between the steady and unsteady contribution of the aerodynamics, which is impossible when the fit is applied to the generalized aerodynamic forces.

It might still be useful to use the classical form of the RFA of the Generalized Aerodynamic Forces (GAFs) $\mathbf{Q}_{hh}$, e.g. for application in p method flutter calculations. The least squares fit

of the "physical" RFA matrices can be converted to the fully generalized form by generalizing the AIC matrices as described in [6].

$$\mathbf{Q}_{hj} = \mathbf{\Phi}_{gh}^{\mathrm{T}}\ \mathbf{T}_{kg}^{\mathrm{T}}\ \mathbf{S}_{kj}\ \mathbf{Q}_{jj} \tag{11}$$

and the two differentiation matrices

$$\mathbf{D^x}_{jh} = \mathbf{D^x}_{jk}\mathbf{T}_{kg}\mathbf{\Phi}_{gh} \ \text{ and } \ \mathbf{D^t}_{jh} = \mathbf{D^t}_{jk}\mathbf{T}_{kg}\mathbf{\Phi}_{gh}. \tag{12}$$

Multiplication and rearrangement of the terms, yields

$$\begin{aligned}\tilde{\mathbf{Q}}_{hh}(\hat{s}) = &\underbrace{\left(\mathbf{Q^0}_{hj}\mathbf{D^x}_{jh}\right)}_{\tilde{\mathbf{Q}}^{\mathbf{0}}_{hh}} + \underbrace{\left(\mathbf{Q^1}_{hj}\mathbf{D^x}_{jh} + \mathbf{Q^0}_{hj}\mathbf{D^t}_{jh} + \sum_{i=1}^{n_p}\mathbf{Q^{L}}_{i\,hj}\mathbf{D^2}_{jh}\right)}_{\tilde{\mathbf{Q}}^{\mathbf{1}}_{hh}}\hat{s} + \underbrace{\left(\mathbf{Q^1}_{hj}\mathbf{D^t}_{jh}\right)}_{\tilde{\mathbf{Q}}^{\mathbf{2}}_{hh}}\hat{s}^2 \\ &+ \sum_{i=1}^{n_p}\underbrace{\left(\mathbf{Q^{L}}_{i\,hj}\left(\mathbf{D^x}_{jh} - \mathbf{D^t}_{jh}\,p_i\right)\right)}_{\tilde{\mathbf{Q}}^{\mathbf{L_i}}_{hh}}\frac{\hat{s}\mathbf{I}}{\hat{s}+p_i}.\end{aligned} \tag{13}$$

It should be noted the amount of lag states generated is dependent how the final unsteady aerodynamic system is realized (physical or fully generalized) and not on the amount of elements of the underlying least squares fit. The generalized form in equation (13) however, does not allow to discern between the steady and unsteady contributions anymore.

When implementing the unsteady aerodynamics in a block diagram, special attention has to be paid to the $\mathbf{Q^1}_{jj}$, respectively $\mathbf{Q^2}_{hh}$ term. These are multiplied with the modal accelerations, as the name added mass suggests. Implementation in e.g. Simulink leads to an algebraic loop breaking or slowing down the simulation immensely. When breaking the loop with a unit delay, linearization of the model is more difficult to achieve. Therefore, advice is to implement the terms as mass term with an explicit inversion.

### 4.4 Sensors and Actuators

The model equations so far only cover the flight physics of the flexible aircraft, i.e. structural dynamics, flight dynamics and aerodynamics. To complete the aircraft model the system aspect, i.e. sensor and actuator dynamics have to be modelled. The sensors are attached to nearest structural grid point with a rigid connection. The IMU sensor equations for the local accelerations and rotation rates are implemented in a similar fashion as derived in [16]. The nose boom was also considered flexible and therefore adds noise due to the elastic motion. Noise, bias and delays were added to all sensors either based on estimation or measurement. The actuators were modelled as second order transfer functions with deflection and rate limits. This way the effects on the control laws when violating these limits could be assessed. With the sensors and actuators in place, the servo loop can be closed with the respective implementations of the control laws. Either in continuous form to test the principles or the discrete implementation to assess quantization effects. For HIL simulations the control laws are running on the actual flight hardware and can be connected to the model and simulated accordingly.

### 4.5 Other Model Components

There are some additional systems that are modelled as discrete forces acting on the airframe. Since the classical DLM does not account for inplane forces, aerodynamic drag is not accounted for. Drag however is important for the flight dynamics of the manoeuvering aircraft and hence for the baseline controller design.

The drag is modelled in the following way. The current lift of the flexible aircraft is calculated. With this lift value, the predefined drag polar is interpolated. The resulting drag force is then applied to the aerodynamic reference point as a concentrated force. This way the impact on the overall flight dynamics was captured, the effect of the inplane forces on the flexibility was considered negligible. Tests with an enhanced DLM also showed no effect of inplane forces on the flutter mechanism either [17].

Next the engine dynamics were implemented as transfer functions with measured delays. Again an important model aspect for design of the baseline controller. Additionally, the first aircraft T-FLEX had an airbrake installed. This airbrake would deflect panels on the fuselage sideways to increase drag. The drag forces wered determine based on deflection angle and airspeed and applied to a structural grid point on the fuselage. The dynamics of the airbrake actuator was also modelled. Since the flight test procedure was later changed from a horse race track to circles with constant radius this system was considered to be superflous. Therefore, the successor aircraft P-FLEX does not have this system, to save weight, system complexity and integration effort.

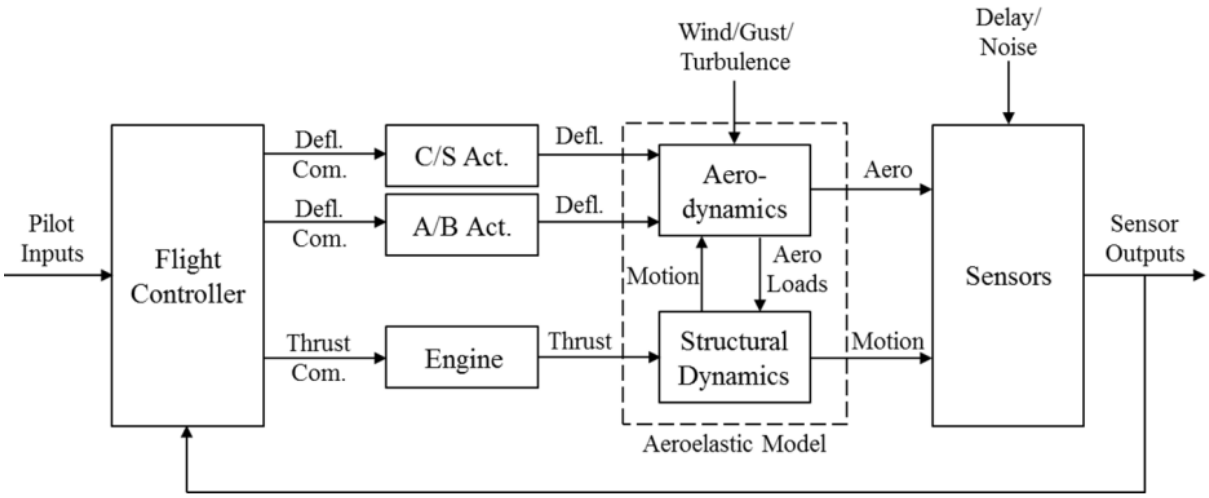


Figure 5: Model components of the integrated model

Figure 5 shows the structure of the model components of the integrated nonlinear simulation model. To provide a rough estimate, the simulation speed of the integrated nonlinear model is approximately real-time capable. This capability varies depending on the number of flexible modes and the number of poles considered for the unsteady aerodynamics.

## 5 FLUTTER ANALYSIS

During the development of the flexible wings for flutter testing, the design target of a flutter speed of around 50 m/s and a flutter frequency of well below 10Hz had to be achieved. These

targets were defined to comply with the visual line of sight requirements and the associated maximum speed of around 60 m/s that could be achieved. Hence, the flutter speed needed to be lower to be within the design envelope. Furthermore, the flutter frequency needed to be low enough to be controllable with the available bandwidth of the actuator as the limiting factor. During the design two flutter mechanism emerged, one symmetric and one antisymmetric flutter mode. Some studies, regarding the placement of the rather heavy actuators were carried out to increase the spacing between those two flutter points, to simplify the control design task. [18, 19]. The flutter analyses during the project were done by employing three methods the p-k method, the p method and the eigenvalue analysis of the nonlinear integrated model, depending on the design task at hand and to cross validate the results.

### 5.1 $p-k$ Method

The $p-k$ method, or "British"-method, is a frequency domain method, which was formulated by Hassig [20]. It is one of the classical frequency domain methods, implemented in many standard aeroelastic flutter tools [21]. The equation to be solved by the $p-k$ method is

$$\left[\mathbf{M}_{hh}\, p^2 + \left(\mathbf{B}_{hh} - q_\infty \tfrac{c_{ref}/2}{V} \operatorname{Im}\left(\mathbf{Q}_{hh}(k)\right) \tfrac{1}{k}\right) p + \left(\mathbf{K}_{hh} - q_\infty \operatorname{Re}\left(\mathbf{Q}_{hh}(k)\right)\right)\right] \mathbf{u}_h = 0. \quad (14)$$

The generalized aerodynamic forces are split into a damping and a stiffness part and subtracted from its structural counterparts accordingly. Since the eigenvalue $p$ is not independent from the reduced frequency $k$, the eigenvalues have to be determined iteratively.

$$k = \tfrac{c_{ref}/2}{V} \operatorname{Im}(p) \quad (15)$$

The interpolation of the GAF matrix ($\mathbf{Q}_{hh}(k)$) is accomplished by a so called Special Linear Interpolation (SLI). I.e., the GAF matrix is interpolated with respect to the reduced frequency $k$ by a cubic radial basis function. The real and imaginary parts are treated separately, where the imaginary part is divided by the reduced frequency before interpolation, to match closely the terms in equation (14). This iteration is repeated for a range of flight velocities resulting in a set of unsorted converged eigenvalues, representing damping and frequencies of the aeroelastic coupled system. When the real part of the eigenvalue becomes positive, flutter occurs. The converged eigenvalues are subsequently tracked and sorted using the Hungarian-method by James Munkres to handle potential mode crossings.

### 5.2 $p$ Method

To avoid the iterations due to the disparity between the values $p$ and $k$ in eq.(15), the so called $p$ method was proposed [14]. The transfer functions of the aerodynamic GAF matrix can be approximated by rational functions, e.g. by Roger's method [9]. With the analytical Laplace transform for rational functions, the GAF matrix can be expressed as an improper state space model by analytical continuation.

$$\mathbf{Q}_{hh}(\hat{s}) = \mathbf{Q^0}_{hh} + \mathbf{Q^1}_{hh}\, \hat{s} + \mathbf{Q^2}_{hh}\, \hat{s}^2 + \mathbf{D}\left(\hat{s}\mathbf{I} - \mathbf{R}\right)^{-1} \mathbf{E}\hat{s} \quad (16)$$

The variable $\hat{s}$ is the Laplace equivalent to the reduced frequency $k$.

$$ik = i\omega \left(\tfrac{c_{ref}/2}{V}\right) \Leftrightarrow \hat{s} = s \left(\tfrac{c_{ref}/2}{V}\right) \quad (17)$$

With this relationship, the equations of motion can then be expressed in the Laplace domain.

$$\left[\mathbf{M}_{hh}\, s^2 + \mathbf{B}_{hh}\, s + \mathbf{K}_{hh} - q_\infty \mathbf{Q}_{hh}(\hat{s})\right] \mathbf{u_h} = 0. \quad (18)$$

Eq. (18) is then cast as a first order ODE in a state space system, where the eigenvalues of the system matrix can be determined directly. This method has its root in control theory and was applied to analyze control laws for an Active Flutter Suppression system [14]. Again, this procedure is repeated for a range of velocities and the modes are tracked by the Hungarian method.

### 5.3 Linearization of the Integrated Nonlinear Model

An alternative to the $p$-method is the linearization of the integrated non-linear model of the flexible aircraft described in the previous section. After a trimming procedure, the model is linearized and the eigenvalues of the system can be determined accordingly. Additional effects, such as linearized direction of gravity, nonlinear drag polar etc. can be accounted for in a straight forward way. As the described modelling scheme also relies on an RFA, it can be considered a special case of the $p$-method. This approach is used to generate the linear models for controller synthesis after some additional model order reduction techniques are applied.

### 5.4 Flutter Analysis of the Demonstrator

This last approach has been used for several studies during the design phase of the demonstrator aircraft and yields almost identical results to the established classical $p$ and $pk$ methods. Also some enhanced doublet lattice methods including body panels and in plane aerodynamic forces have been considered [17]. An example of a pole migration is shown in figure 6. As the

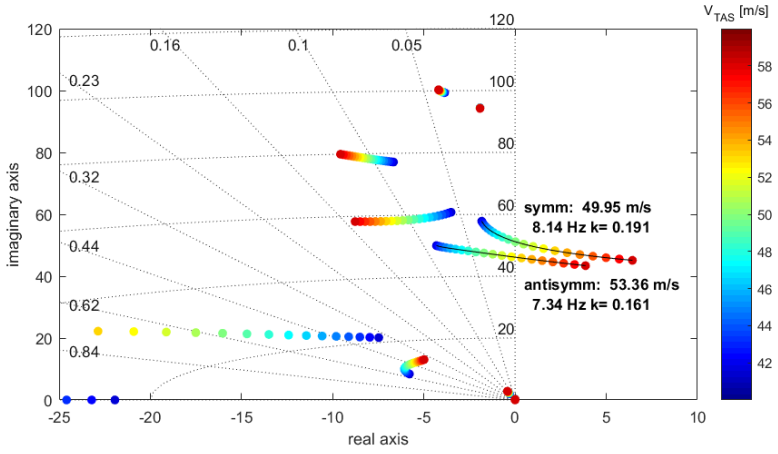


Figure 6: flutter poles

data bases for stiffness and mass matured, the flutter speeds converged to around 50 m/s for the symmetric flutter mode and around 53 m/s for the antisymmetric flutter. Also the flutter mechanisms and the modal contributions varied only slightly along the development axis and were confirmed by multiple partners. Figure 7 shows the evolution of the modal contributions over the flight velocity using the computational model. For the first flutter mode the symmetric torsion mode (9) couples with the first symmetric bending mode (7). Also the second symmetric bending is present (11), as well as the rigid body heave (3) and pitch (5) mode. The rigid body modes were computed using a principal inertial axes system and were mass normalized. For the antisymmetric flutter mode, the first antisymmetric bending (8) couples with the antisymmetric torsion (10). Also a significant contribution stems from the rigid body rolling mode (4).

This status of the model was then used for controller design. As will be show later some significant changes arose from the test data of the ground vibration test.

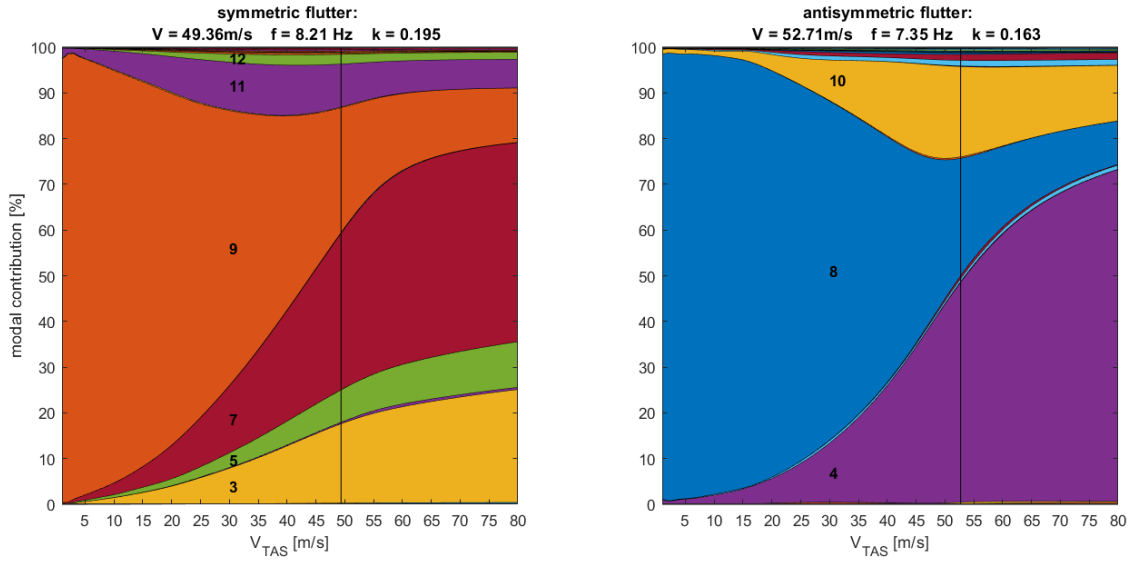


Figure 7: modal contributions over velocity of the critical flutter modes (FEM model)

## 6 MODELLING FOR CONTROLLER DESIGN AND VALIDATION

The flight control design task typically requires linear state space models of low order. Hence the high dimensional models of elastic aircraft with many states related to unsteady aerodynamics must be reduced to facilitate the various design methods. The resulting models yet have to cover the important physical effects for the corresponding application.

### 6.1 Baseline Controller

The baseline flight control system is designed to navigate the aircraft fully autonomously around the predefined flight test track. The architecture of the baseline controller to augment the rigid body motion, features a classical cascaded flight controller architecture [22,23] with well proven feedback loops of proportional-integral-derivative (PID) controllers together with damping augmentation. These control loops provide capabilities for augmented pilot-in-the-loop flights as well as for autonomous flights. More details on the design of the baseline controller and its different modes of operation can be found in [24]. Flight dynamics models for the design tasks above do not require unsteady aerodynamics, as the dynamics are typically slow and no substantial effect is to be expected. Furthermore, the flexibility effects are usually modelled by augmenting the aerodynamic database with so called flexible factors. Here an alternative approach is proposed. To account for flexible aerodynamic effects the additional states due to structural dynamics can be omitted by assumingthe modal acelerations and velocities are zero. Then, the external forces due to rigidbody aerodynamics, control surface deflections, thrust of the engine and any other source $\mathbf{P}_g^{\text{ext}}$ are summed up and generalized with the flexible mode matrix.

$$\mathbf{P}_f^{\text{ext}} = \mathbf{\Phi}_{gf}^T \mathbf{P}_g^{\text{ext}} \tag{19}$$

The generalized Aerodynamic Force Matrix for the flexible modes $\mathbf{Q}_{ff}$ is the used to compute the flexible deformation $\mathbf{u}_f$ including the aeroelastic effects.

$$\mathbf{u}_f = (\mathbf{K}_{ff} - q_\infty \mathbf{Q}_{ff})^{-1} \cdot \mathbf{P}_f^{\text{ext}} \tag{20}$$

This flexible deformation can be in turn used to calculate the distributed aerodynamic forces due flexibility.

$$\mathbf{P}_g^{\text{flex}} = \mathbf{Q}_{gj} \mathbf{D}^{\mathbf{x}}{}_{jk} \mathbf{T}_{kg} \mathbf{\Phi}_{gf} \mathbf{u}_f \tag{21}$$

This way the typical 12 state rigid body model can be set up. Important for a flight dynamics model is the application of a drag polar and to account for a direction of lift perpendicular to the onflow. These are usually not covered by aeroelastic models, cf. [25]. Furthermore, the engine dynamics play an important role and should be modelled accurately with the associated dynamics. The trimmed and resulting linearized models can be used in conjunction with the nonlinear simulation model to design the baseline flight control laws.

### 6.2 Active Flutter Suppression Control Laws DLR

For the design of the active flutter suppression control laws, the DLR chose an $H_2$ optimal input output blending method. This approach is particularly suitable, since the order reduction requirement of the typically high dimensional aeroelastic model can be somewhat relaxed. The model for the control synthesis of this blending method is obtained by directly linearizing the full nonlinear model about trim states at a predefined velocity points. The next step is to extract a linearized model at a velocity that exceeds the flutter velocity, around 60 m/s. This ensures that the model captures the dynamics of the aircraft in the region where flutter is likely to occur, providing a basis for designing the flutter suppression controller. Initially, the linearized model is blended to distinguish between the symmetric and asymmetric flutter mechanism. To manage the complexity of the model, model reduction techniques such as minimum realization with the balred function in MATLAB can be employed. As stated before this requirement can be somewhat relaxed but eases the synthesis process. The simplified model is then converted to the canonical realization form and used for design of the blending vectors for the asymmetric and symmetric flutter modes. Then notch filters are applied to the two Single Input Single Output (SISO) loops to attenuate high frequencies and avoid interference with the dynamics of the low-frequency baseline controller. The blending vectors and notch filters designed for the critical velocity are extended to the linear models across all velocity points. Importantly, the blending vectors and notch filters are kept constant for all velocities, ensuring consistency in the control strategy across the operational speed range. Finally, the SISO loops are tuned using the $H_\infty$ technique. A gain scheduling of the obtained parameters is then performed over the corresponding velocity. This robust control method ensures adequate stability margins (disk margins), which are crucial for effective flutter suppression.

### 6.3 Active Flutter Suppression Control Laws SZTAKI

The flutter controller developed by SZTAKI aims to mitigate the undamped oscillations of the wings that occur if the aircraft is flying beyond the flutter speed [26, 27]. It uses the outermost aileron pair to achieve this goal. The design objectives for flutter suppression are to achieve robust stabilization in the presence of mixed uncertainty. The method used alternates between an analysis step and a synthesis step. Samples of the parametric uncertainty are computed during the analysis steps, thus yielding an array of uncertain systems containing only dynamic uncertainty. The controller is then synthesized on this array of uncertain models. This synthesis step itself involves an alternation between constructing a D-scale for each of the uncertain systems and tuning a single controller for the entire collection of scaled plants. The controller tuning is performed using structured control design techniques.

The reduced order model used by SZTAKI for the synthesis was obtained by using a bottom-up modelling approach. The bottom-up modeling is pursued in order to obtain an LPV model of the FLEXOP aircraft that is of sufficiently low order for control design. The key idea is to reduce the subsystems before the integration into the nonlinear model. The reason behind this is that the structural dynamics and aerodynamics subsystems have simpler structure than the combined

ASE model. Thus, the order of these subsystems can be reduced by simpler and more tractable reduction techniques. Such approach leads to a low order ASE model (LOM). Further details on the bottom up modelling approach and the individual reduction of the subcomponents of the simulation model can be found in [26, 28].

### 6.4 Validation of Control Laws in Nonlinear Simulation

For implementation of the control laws on the Flight Control Computer hardware, it is necessary to convert the continuous-time control law to a discrete-time equivalent. The discretized controllers are then integrated into the nonlinear simulation. To validate the correct behavior of the control laws, simulations of the test flight scenarios are carried out. Focus here is on the validation of the autopilot modes and the active flutter suppression systems. The test flight scenario for acquiring this stationary test point was initially a horse race track pattern, i.e. accelerating the aircraft to a certain speed, brake, turn and reposition the aircraft for the next selected speed. This procedure was later revised in favor of a circle with constant radius as this allowed to collect stationary data over a longer period of time. This improved the identification of the modal parameters by the onboard system and also in post flight analysis considerably. The software in the loop simulation (SIL) in figure 8 shows how the velocity is successively increased while flying in circles with a constant radius of around 800m. The first two times the flutter control law was active. The control surface activity of left and right outboard flaps 4 stay well below 0.5 deg and stabilize the symmetric flutter mode until at times 35 s and 70 s. Then the symmetric flutter occurs with a speed of around 63.5 m/s. The third and fourth time the speed is increased with the flutter control laws switched off, hence the outboard flaps 4 remain in neutral position. At 86 s and 122 s the symmetric flutter mode goes unstable at a speed of around 55.5 m/s. The software in the loop simulation was successfully able to demonstrate that the flutter control law is substantially increasing the flutter free flight envelope. The modal deflections at both open loop and closed loop flutter points show a contribution of the first symmetric wing bending and torsion, as well as the second symmetric bending, which is in line with the flutter analyses.

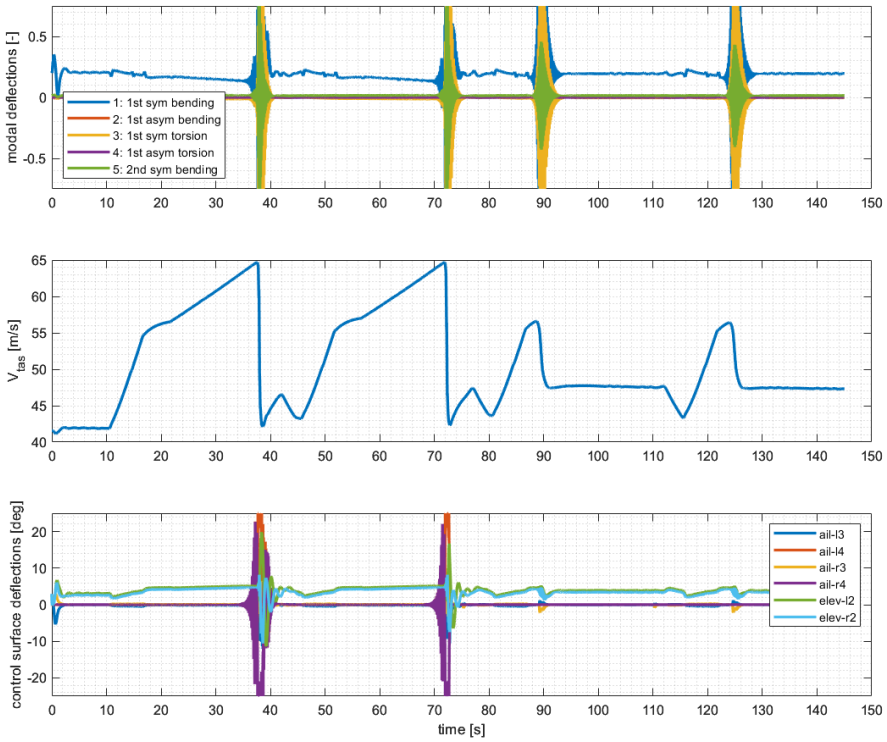


Figure 8: Integrated Software in the Loop Simulation of the flutter and baseline controller

## 7 MODELLING AND GROUND TESTING

During the development of the demonstrator aircraft, extensive ground testing activities were conducted. These activities are described in detail in [29]. This section points out some of these tests related to obtain valuable test data to update the simulation models, as well as some test which required dedicated mathematical models to conduct these tests. One of the earlier test conducted was a static load test, where the wings were mounted on a test rig. Then specific loads were introduced with load clamps and the resulting deflections were measured [29]. The obtained static deflection data was used to update the FEM model stiffness parameters. The jet engine B300F and the pylon mounted onboard thrust measurement system was tested [30] at the Technical University of Munich. The determined engine characteristics were used to update the dynamic model of the jet engine. The custom build direct drive flutter actuator including their internal control laws was tested and its dynamic behavior under load was identified [26]. The results were used to update the transfer functions for the outboard flaps 4 of the nonlinear simulation model. The same procedure was employed for the off the shelf actuator MKS HBL 599. This actuator type is installed on the remaining aerodynamic control surfaces. Compared to the flutter actuator, these had less demanding requirements. These tests were done to confirm the specifications of the data sheets and update the dynamic models.

### 7.1 Hardware in the Loop Testing

Before conducting Hardware in the Loop (HIL) tests, implementation of both controllers (baseline and flutter) on the real FCC hardware was performed. All of the controllers are constructed in Matlab / Simulink as discrete time models with 5ms sampling and the executable code is built from this after SIL test runs prove the correct functionality of the controllers. Of particular importance are the delay times in the actual hardware components, which have direct ramifications on the stability properties and the controller design. The hardware delay was 15 ms, which served as input for the control law synthesis. In the HIL test the FCC and the auxiliary hardware with the implemented control laws was then coupled to the simulation model of the aircraft including the actuator and sensor dynamics. The aircraft could be flown virtually using the radio transmitters with a Flightgear desktop visualization as shown in figure 9. Various tests of the baseline controller modes, different flutter control laws with varying delays have been conducted. More details can be found in [26].

From a simulation model perspective, the HIL scenario was particularly challenging because of the requirement for a real time capable model execution, while still capturing the physics of the flutter characteristics. Careful selection of the modes and the order of the unsteady lag states allowed to comply with these requirements.

### 7.2 Ground Vibration Test

The GVT is a modal test which is generally used to identify resonance frequencies, damping ratios and mode shapes of aircraft structures on the ground before the first flight of a prototype. The results are either used to validate and update the Finite Element (FE) model for further aeroelastic simulations and final flutter clearance or the identified modal model can be used directly for flutter calculations. The GVT of the FLIPASED aircraft was conducted by a team from ONERA and DLR at the DLR Institute of Aeroelasticity in Göttingen. The aircraft was then instrumented with approximately 150 lightweight accelerometers including uni-axial and tri-axial sensors. These provide the benefit of not mass loading the structure, while maintaining high accuracy even at low frequencies. Several electro-dynamic shakers were used to excite the structure with different custom designed input signals, cf. figure 10.

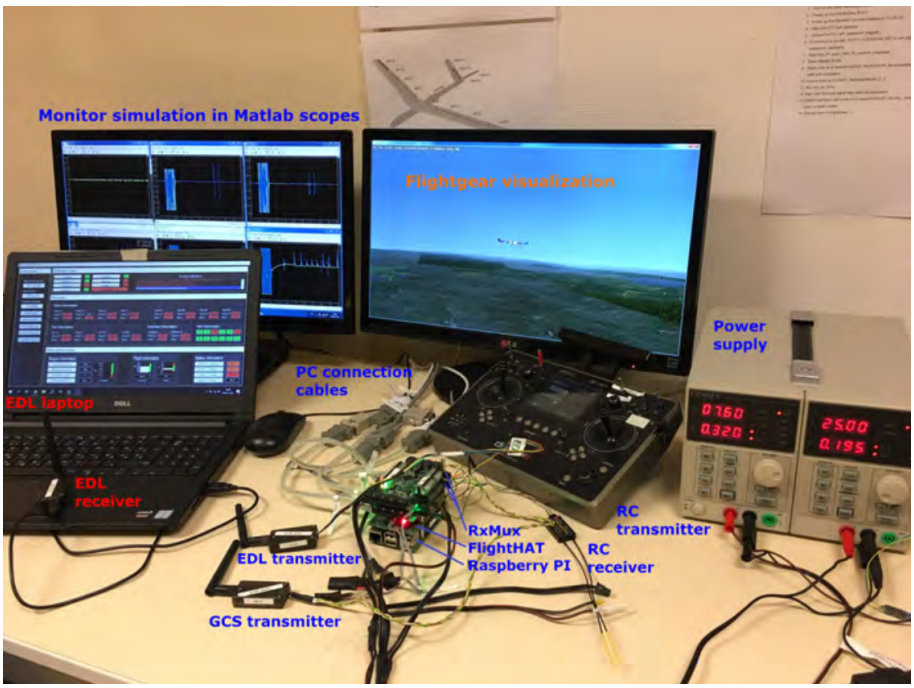


Figure 9: HIL simulation setup

Figure 10: GVT test setup

An extensive test campaign was carried out with the flutter prone wings of the newly build second demonstrator aircraft P-FLEX. Several configurations were tested, most importantly the flutter configuration with the flutter rods mass loaded (flutter prone configuration C1a) and flutter stopper released, where the masses are moved forward towards the trailing edge (flutter free configuration C1b). For more detailed information on the GVT procedure and the outcomes obtained, please refer to FliPASED project deliverable D3.9 [31]. This report provides comprehensive insights into the GVT process, including the methodology, instrumentation, data collection, and analysis techniques utilized. In the following paragraphs, only the results of the flutter prone configuration are presented. The frequency and damping values of the modes and their respective sorting are shown in table 1 for the FEM model and the GVT results. Some modes are not present in FEM model, e.g the wing inplane modes. The tail rock mode vastly differ between the FEM and the GVT in terms of shape and frequency. The symmetric modes are well represented. The antisymmetric show more difference between model and test.

Table 1: Modal frequencies and damping: FEM model vs GVT results

| | **FEM** | | | **GVT** | | |
|---|---|---|---|---|---|---|
| mode description | mode | $f$ [Hz] | $g$ [%] | mode | $f$ [Hz] | $g$ [%] |
| 2n_wing_bend-s | 7 | 2.899 | 1.0 | 6 | 2.938 | 1.10 |
| 3n_wing_bend-a | 8 | 8.156 | 1.0 | 7 | 7.220 | 0.79 |
| 1n_wing_inplane-a | | | | 8 | 8.491 | 1.83 |
| wing_tors-s | 9 | 10.608 | 2.0 | 9 | 10.744 | 0.95 |
| wing_tors-a | 10 | 10.717 | 2.0 | 10 | 11.155 | 1.07 |
| 4n_bending-s | 11 | 12.134 | 2.0 | 11 | 12.023 | 0.72 |
| 2n_wing_inplane-s | 12 | 14.953 | 2.0 | 13 | 14.846 | 1.19 |
| v-tail_rock | 13 | 15.694 | 2.0 | 12 | 12.501 | 3.36 |
| 5n_wing_bend-a | 14 | 19.482 | 2.0 | 17 | 20.383 | 1.78 |
| bending-a | 15 | 23.684 | 2.0 | | | |
| 6n_wing_bend-s | 16 | 24.511 | 2.0 | 20 | 25.860 | 1.82 |

## 8 FLIGHT TEST CLEARANCE

Flight testing of the active flutter suppression system was the culmination of the project. It was important to ensure the accuracy of the aeroservoelastic simulation model and that changes in the dynamic structural properties would not affect the performance of the flutter control laws before flight testing began.

It turned out that despite the fact that the frequencies between the model and the GVT test results matched quite well (in particular for the modes involved in the critical symmetric flutter mechanism 7,9 and 11, c.f. 7), the modal masses of the torsional modes were off. The modal mass is related to the magnitude of the mode shapes, and those were overestimated by the FE model. This can have a substantial influence on the flutter speeds. Since the time between the evaluation of the GVT data and the upcoming flight test was short, it was decided to use the identified modal model for the flight test clearance. The measurement locations were mapped to the structural grid points of the FEM in a similar fashion to the interpolation between the aerodynamic grid and the structural grid in the regular modelling process. With the GVT mode shapes available on the FEM grid, the same AIC matrices could be used for the subsequent flutter calculation. Due to this modal mass effect, a surprisingly large shift in flutter speeds occurred. The symmetric flutter mode shifted from 50 m/s to 55.5 m/s. The antisymmetric flutter shifted even more from 53 m/s to 78 m/s, well outside of the flight envelope of the demon-

strator. This large shift can be partially attributed to the increased frequency separation of the antisymmetric 1st bending and 1st torsion mode. This flutter analysis was confirmed independently by different partners with different analysis methods. The overall flutter mechanisms and frequencies however did not change, c.f. figure 11.

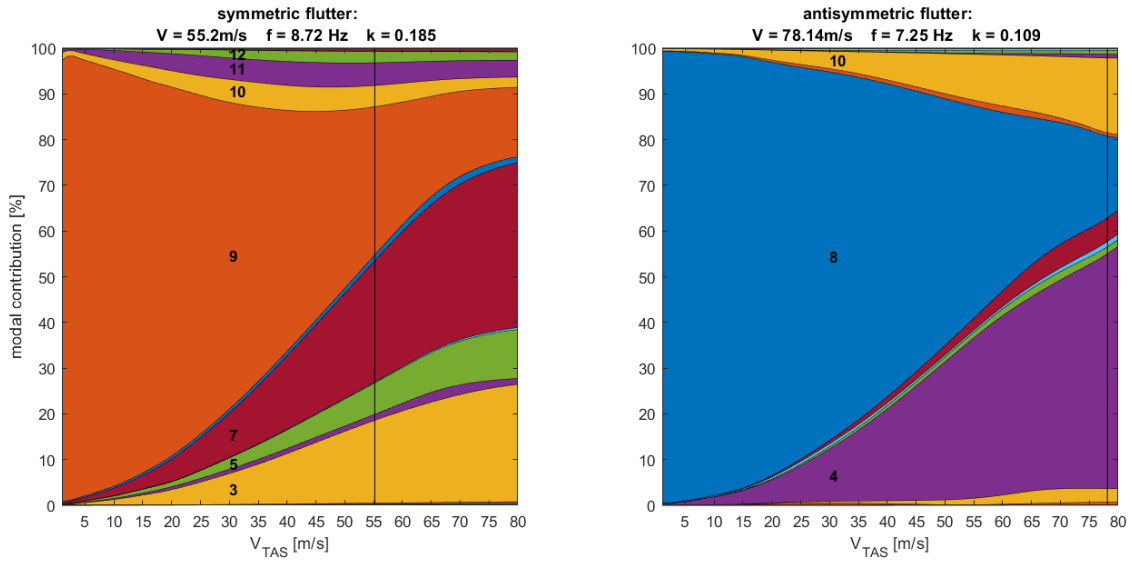


Figure 11: modal contributions over velocity of the critical flutter modes (GVT model)

### 8.1 Flight Test Clearance of AFS Control Laws

For the $p$ method flutter analysis with GVT updated modal parameters, a series of state space models for the different velocities were generated. To clear the flutter control laws for flight, these models were coupled as a linear parameter varying (LPV) representation to the linear flutter control laws in order to verify the desired behavior. Despite the rather large changes in flutter velocities, it could be confirmed by frequency and time domain analyses that both control laws from DLR and SZTAKI were able to delay the flutter well beyond 60 m/s. Therefore, the decision was made to proceed with the flutter flight tests the next day.

### 8.2 Subcritical Flight Test Below Open Loop Flutter Speed

The flight test FT32 was planned to slowly approach the predicted flutter speed without the AFS controllers active. Steady circles with a radius of 800m at an altitude (ALT) of ca. 360 m were flown. The velocity was incrementally increased 44 m/s to 54 m/s. During the flight test, the modal parameters were closely monitored using an Online Modal Analysis system implemented onboard on a secondary flight computer. Details about the system are described in [32]. After the successful flight, the online identified modal parameters were verified and additionally post flight analysis of the damping and frequency values was conducted. The parameters of both analyses agreed very well and confirmed that the system is working as expected. Figure 12 show the post flight analysis values of the identified modal frequencies and damping trends for the flight points 44, 46, 48, 50, 52, 53 and 54 m/s. These values are compared to the GVT verified state space models used in the p method flutter analysis. The agreement between the model and the test data is excellent. In particular the damping trend of the critical flutter mode is well captured and confirms the expected open loop flutter to occur around 55 m/s. As the velocity approaches the flutter speed, the flutter mode is getting dominant and the damping decreases to almost zero. The tracking of the other modes is lost for the final test points closest to the flutter speed. This is in line with the findings in [33], where this effect was shown with

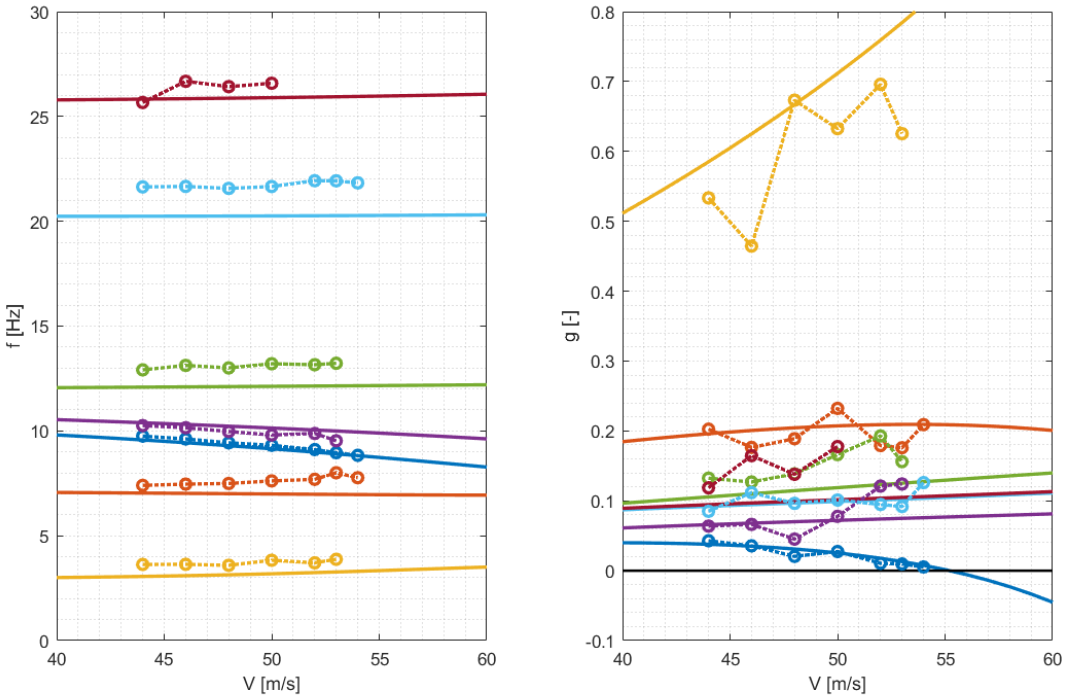


Figure 12: modal frequency and damping over velocity: Simulation model (solid) vs. post flight analysis values of flight test points (dotted)

synthetic test data. In the next flight tests FT 33 and FT 34, the flutter controllers were switched on in subcritical conditions. Steady circles with 44, 48 and 50 m/s were flown. For each velocity point the controller was switched off for 90 s followed by a segment of 90 s, where the flutter controller was active, before increasing the velocity. The DLR controller was tested in FT33 and the SZTAKI controller in FT34. Both controllers were increasing the damping of the wing torsional mode.

### 8.3 Critical flight tests beyond open loop flutter speed

May 26th was the final flight day of the project and the performance of the active flutter was tested beyond the open loop flutter speed. This was the culmination of a several years long effort to demonstrate active flutter suppression for a conventional flutter mechanism in flight. Once more, two successive flights were planned, one for each flutter controller FT 35 (DLR controller) and FT 36 (SZTAKI controller). The flights were done with the flutter control law alternating between off and active for circles with 50 and 54 m/s as shown in figure 13. After that the controllers remained active, for the flight points 55, 56, 57, 58, 59 m/s. In guts the velocity peaked at 62 m/s. The aircraft remained stable for both controllers, successfully showing that active flutter control works.

Figure 14 show the frequency domain analysis of the critical velocity of 54 m/s. Clearly visible is the peak at the flutter frequency of around 8.8 Hz for the IMU output at the outermost (90% span) stations. With the AFS control law active, the control surface shows most activity at this frequency, effectively flattening the peak and preventing flutter.

The final flight of the demonstrator was FT 37 to confirm the open loop flutter speed. Therefore, the velocity was gradually increased beyond the calculated flutter speed, while closely monitor-

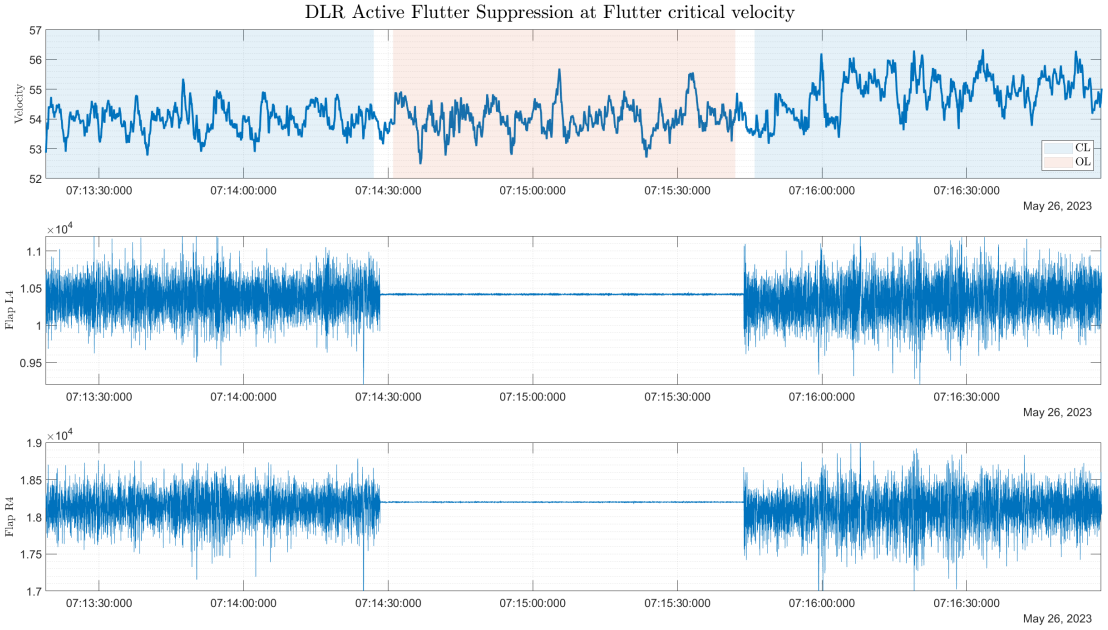


Figure 13: FT35 Time domain plot of the control surface activity at speed 54 m/s with the active flutter suppression switched on and off before advancing to 55 m/s.

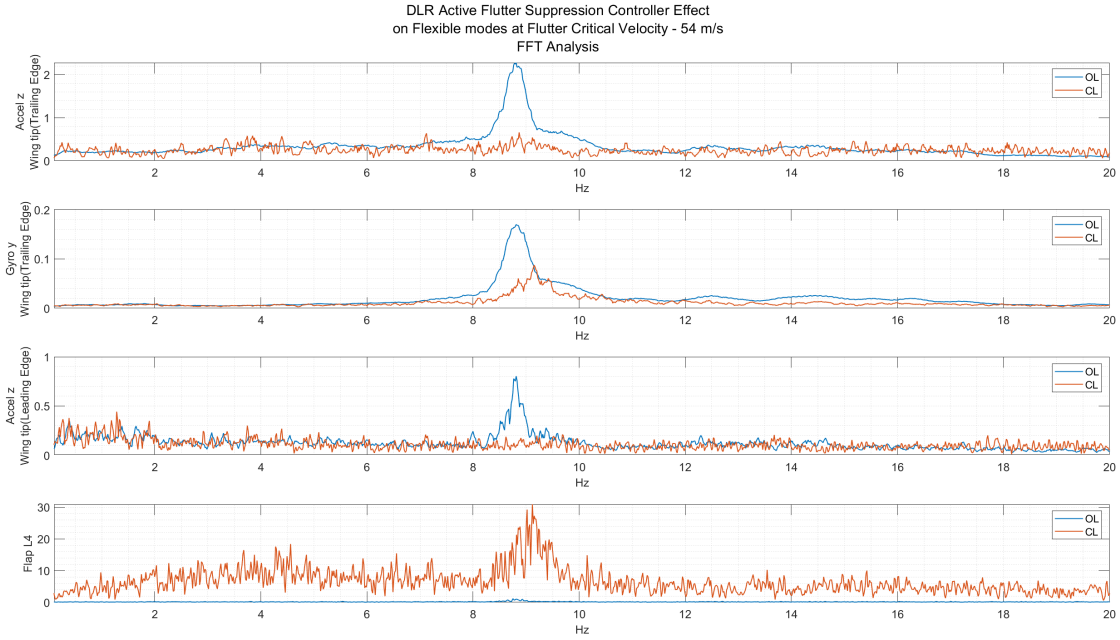


Figure 14: Frequency domain analysis at speed 54 m/s with the active flutter suppression on and off.

ing the modal damping parameters with the OMA system. Eventually, the flutter stoppers were to be released to prevent the aircraft from crashing. Between 55 and 57 m/s the flutter rod broke off unnoticed, changing the flutter behavior to an uncritical configuration. When it was detected that the flutter rod is missing, the flight test was aborted and the aircraft landed safely. Although the test was not according to plan, nevertheless post flight analysis confirmed the flutter speed as predicted by the model.

## 9 CONCLUSION

Modeling is inherently an abstraction of reality, and a model must accurately represent specific aspects of this reality to effectively answer analytical questions related to those aspects. Depending on the objectives of a particular analysis, the underlying equations of the model integration might be different. Also, the validity range might depend on how and which data is selected to be incorporated in the model. Furthermore, it is crucial to recognize the limitations of the underlying theories and experimental methods used to develop mathematical models. Both experimental and computational data must be rigorously scrutinized in this context.

The overall objective of the two projects FLEXOP and FliPASED was to demonstrate an active flutter suppression system in flight, beyond open loop flutter speed, with a conventional wing bending-torsion flutter mechanism. To support these goals efficient simulation models have been provided for various design tasks. The proposed integrated modelling process demonstrated its ability to support all kinds of design analyses thanks to its modular approach. All models were fed by the same underlying data ensuring consistency between the models for the different applications.

Several examples of models used along the development axis of the project and for the various design analyses have been presented. Most importantly for flutter analysis and models for control synthesis. Control law design for the baseline controller, required low order nonlinear flight dynamics models of the manoeuvering aircraft including drag and engine characteristics. The design of the flutter suppression control laws required an accurate representation of the structural dynamics and unsteady aerodynamics. The interaction of the control laws needed to be assessed, requiring an integrated simulation model representing both the slow dynamics of the nonlinear manoeuvering aircraft and the flexible dynamics including unsteady aerodynamics. The assessment was then conducted in SIL simulations of the intended flight test scenarios. Furthermore, these control laws were implemented on flight hardware and have been tested HIL simulations, to verify the correct implementation in the real life environment.

In the phase immediately before the critical flight tests, the project was taken by surprise. Despite the fact that the modal frequencies agreed well between the FEM model and the GVT, the overestimated modal masses, i.e. magnitudes of the mode shapes, had a significant and unexpected impact on the flutter speeds. The flutter speed for the critical flutter mode increased from 50 m/s to around 55.5 m/s. The take away message is to not only verify the frequencies and shapes of the modes of the GVT, but also pay attention to the modal mass. This could serve as an important uncertainty parameter when certifying active flutter suppression systems in the future.

Taking these findings into account, GVT updated models were used for pre-flight flutter analyses and the flight test clearance of the implemented active flutter suppression control laws.

Although, not resynthesized with an updated model, the control laws worked well in the test flights. Partly because the robustness was a dedicated design goal, but also because the flutter

frequency and mechanisms have remained the same. Further investigations on the robustness and performance of the control laws still need to be conducted. Also, to assess to what extend the retuning of the control law with updated models would have improved the performance.

The online monitoring as well as the post-flight analysis of the modal frequency and damping parameters proved to be an invaluable tool to validate the simulation model. Excellent agreement between the GVT updated model and the flight test data could be shown. This build the confidence in the model to test the active flutter control laws in flight beyond open loop flutter speed.

The flight tests of both control laws successfully demonstrated a flutter free envelope expansion of over 10%. Finally, the open loop flutter speed was confirmed in the final test flight, successfully concluding the project. All flight test data and the GVT results are publicly available [31, 34].

The dynamic aircraft model integration process presented in this paper provided consistent simulation models for all kind of design analysis tasks. The aeroservoelastic models and the active flutter suppression control laws have been successfully validated with flight test data.

## 10 ACKNOWLEDGEMENTS

The work presented has been conducted within the framework of projects FLEXOP (grant agreement No. 636307) and FliPASED (grant agreement No. 815058) funded from the European Union's Horizon 2020 research and innovation program.

## 11 REFERENCES

[1] Roessler, C., Stahl, P., Sendner, F., et al. (2019). Aircraft design and testing of flexop unmanned flying demonstrator to test load alleviation and flutter suppression of high aspect ratio flexible wings. In *AIAA Scitech 2019 Forum*. American Institute of Aeronautics and Astronautics. doi:10.2514/6.2019-1813.

[2] Kier, T., Looye, G., Scharpenberg, M., et al. (2007). Process, Methods and Tools for Flexible Aircraft Flight Dynamics Model Integration. In *International Forum on Aeroelasticity and Structural Dynamics*, IF-060. CEAS/AIAA.

[3] Guyan, R. J. (1965). Reduction of stiffness and mass matrices. *Journal of Aircraft*, 3(2), 380. doi:10.2514/3.2874.

[4] Meddaikar, Y. M., Dillinger, J., Klimmek, T., et al. (2019). Aircraft Aeroservoelastic Modelling of the FLEXOP Unmanned Flying Demonstrator. In *AIAA Scitech 2019 Forum*. American Institute of Aeronautics and Astronautics. doi:10.2514/6.2019-1815.

[5] Hofstee, J., Kier, T., Cerulli, C., et al. (2003). A Variable, Fully Flexible Dynamic Response Tool for Special Investigations (VarLoads). In *International Forum on Aeroelasticity and Structural Dynamics*.

[6] Kier, T. M. and Looye, G. H. N. (2009). Unifying Manoeuvre and Gust Loads Analysis. In *International Forum on Aeroelasticity and Structural Dynamics*, IFASD-2009-106.

[7] Waszak, M. R. and Schmidt, D. K. (1986). On the flight dynamics of aeroelastic vehicles. In *AIAA Atmospheric Flight Mechanics Conference*, AIAA 86-2077. AIAA, pp. 120–133. doi:10.2514/6.1986-2077.

[8] M. R. Waszak and D. K. Schmidt (1988). Flight Dynamics of Aeroelastic Vehicles. *Journal of Aircraft*, 25(6), 563–571. doi:10.2514/3.45623.

[9] Roger, K. L. (1977). Airplane Math Modeling Methods for Active Control Design. In *AGARD Structures and Materials Panel*, AGARD/CP-228. AGARD, pp. 4–1 – 4–11.

[10] Pistolesi, E. (1937). Betrachtungen über die gegenseitige Beeinflussung von Tragflügelsystemen. In *Gesammelte Vorträge der Hauptversammlung 1937 der Lilienthal Gesellschaft*.

[11] Harder, R. and Desmarais, R. (1972). Interpolation Using Surface Splines. *Journal of Aircraft*, 9(2), 189–191. doi:10.2514/3.44330.

[12] Rodden, W., Taylor, P., and Jr., S. M. (1998). Further refinement of the subsonic doublet-lattice method. *Journal of Aircraft*, 9(10), 693–702. doi:10.2514/2.2382.

[13] Edwards, J. W. (1979). Applications of Laplace transform methods to airfoil motion and stability calculations. In *20th Structures, Structural Dynamics and Materials Conference*, AIAA 1979-772. doi:10.2514/6.1979-772.

[14] Abel, I. (1979). An analytical technique for predicting the characteristics of a flexible wing equipped with an active flutter-suppression system and comparison with wind-tunnel data. Tech. Rep. NASA TP-1367, NASA LARC.

[15] Kier, T. (2011). An Integrated Loads Analysis Model including Unsteady Aerodynamic Effects for Position and Attitude dependent Gust Fields. In *International Forum on Aeroelasticity and Structural Dynamics*, IFASD-2011-052.

[16] Grauer, J. A. and Boucher, M. J. (2018). Output measurement equations for flexible aircraft flight dynamics. Tech. Rep. NASA TM-2018–220102, NASA.

[17] Kier, T. M. (2023). Comparing different potential flow methods for unsteady aerodynamic modelling of a flutter demonstrator aircraft. In *AIAA SCITECH 2023 Forum*. American Institute of Aeronautics and Astronautics. doi:10.2514/6.2023-0177.

[18] Wüstenhagen, M., Kier, T., Meddaikar, Y. M., et al. (2018). Aeroservoelastic Modeling and Analysis of a Highly Flexible Flutter Demonstrator. In *2018 Atmospheric Flight Mechanics Conference*. American Institute of Aeronautics and Astronautics. doi:10.2514/6.2018-3150.

[19] Wüstenhagen, M., Özge Süelözgen, Ackermann, L., et al. (2021). Validation and Update of an Aeroservoelastic Model based on Flight Test Data. In *2021 IEEE Aerospace Conference (50100)*. IEEE. doi:10.1109/aero50100.2021.9438354.

[20] Hassig, H. J. (1971). An approximate true damping solution of the flutter equation by determinant iteration. *Journal of Aircraft*, 8(11), 885–889. doi:10.2514/3.44311.

[21] Rodden, W. P., Harder, R. L., and Bellinger, E. D. (1979). Aeroelastic Addition to NASTRAN. Tech. Rep. NASA CR-3094, NASA.

[22] Brockhaus, R., Alles, W., and Luckner, R. (2011). *Flugregelung*. Springer, 3. ed.

[23] Stevens, B., Lewis, F., and Johnson, E. N. (2016). *Aircraft Control and Simulation*. John Wiley & Sons, Inc., 3. ed.

[24] Pusch, M., Ossmann, D., and Luspay, T. (2019). Structured Control Design for a Highly Flexible Flutter Demonstrator. *Aerospace*, 6(3), 27. doi:10.3390/aerospace6030027.

[25] Kier, T. (2022). An Integral Flexible Aircraft Model for Optimal Control Surface Scheduling of Manoeuvre Load Alleviation and Wing Shape Control Functions. In *International Forum on Aeroelasticity and Structural Dynamics, 13-17 June 2022, Madrid, Spain*, IFASD-2022-093.

[26] Takarics, B., Patartics, B., Luspay, T., et al. (2020). Active flutter mitigation testing on the FLEXOP demonstrator aircraft. In *AIAA Scitech 2020 Forum*, AIAA 2020-1970. American Institute of Aeronautics and Astronautics. doi:10.2514/6.2020-1970.

[27] Patartics, B., Liptak, G., Luspay, T., et al. (2022). Application of structured robust synthesis for flexible aircraft flutter suppression. *IEEE Transactions on Control Systems Technology*, 30(1), 311–325. ISSN 2374-0159. doi:10.1109/tcst.2021.3066096.

[28] Takarics, B., Vanek, B., Kotikalpudi, A., et al. (2018). Flight control oriented bottom-up nonlinear modeling of aeroelastic vehicles. In *IEEE AeroConf, Yellowstone Conference Center, Big Sky, Montana, USA, Mar 3 - Mar 10, 2018*, 2307-09.0413. doi:10.1109/AERO.2018.8396537.

[29] Sodja, J., Breuker, R. D., Meddaikar, Y. M., et al. (2020). Ground testing of the FLEXOP demonstrator aircraft. In *AIAA Scitech 2020 Forum*. American Institute of Aeronautics and Astronautics. doi:10.2514/6.2020-1968.

[30] Bartasevicius, J., Fleig, P. A., Metzner, A., et al. (2022). Design and testing of an in-flight thrust measurement system for a pylon-mounted miniature jet engine. In *AIAA SCITECH 2022 Forum*. American Institute of Aeronautics and Astronautics. doi:10.2514/6.2022-1827.

[31] Yu, F., Teubl, D., Toth, S., et al. (2019). Advanced Wing Integration and Ground Test. Tech. Rep. D 3.9, FliPASED. Https://flipased.eu/deliverables/.

[32] Soal, K., Volkmar, R., Thiem, C., et al. (2023). Flight vibration testing of the t-flex uav using online modal analysis. In *AIAA SCITECH 2023 Forum*. American Institute of Aeronautics and Astronautics. doi:10.2514/6.2023-0373.

[33] Özge Süelözgen and Wüstenhagen, M. (2019). Operational Modal Analysis for Simulated Flightflutter Test of an Unconventional Aircraft. In *International Forum on Aeroelasticity and Structural Dynamics, Savannah, GA, USA*, IFASD-2019-129.

[34] Bartasevicius, J., Teubl, D., Seren, T., et al. (2023). FliPASED Flight test data. doi:21.15109/CONCORDA/PU4R32.

## COPYRIGHT STATEMENT